First Measurement of Drift-Alfvén Wave Polarization in Magnetically Confined Fusion Plasmas

Xiaodi Du[1,*] Liu Chen,[2,3,4] William W. Heidbrink,[2] Michael A. Van Zeeland,[1]
Max E. Austin,[5] Jie Chen,[6] Yueqiang Liu[1]
George R. McKee[7] and Zheng Yan[7]

[1]*General Atomics, P.O. Box 85608, San Diego, California 92186-5608, USA*
[2]*University of California, Irvine, California 92697, USA*
[3]*National Central University, Zhongli, Taoyuan 320317, Taiwan, Republic of China*
[4]*Center for Nonlinear Plasma Science, ENEA, Frascati 00044, Italy*
[5]*University of Texas-Austin, Austin, Texas 78712, USA*
[6]*University of California, Los Angeles, California 90095, USA*
[7]*University of Wisconsin-Madison, Madison, Wisconsin 53706-1687, USA*

Polarization of drift-Alfvén waves, defined as the ratio of electrostatic to electromagnetic fluctuations, has remained unmeasurable in fusion plasmas for decades, despite its pivotal role in understanding wave dynamics and their impact on plasmas. We report the first measurements of drift-Alfvén wave polarization in a hot, magnetically confined plasma. The breakthrough is enabled by a novel methodology developed from gyrokinetic theory, utilizing fluctuations of electron temperature and density. Analysis of data from the DIII-D tokamak reveals that the waves above the geodesic acoustic mode frequency exhibit dominant electromagnetic polarization, whereas lower-frequency waves show a mix of electromagnetic and electrostatic polarization, indicating a strong coupling between shear Alfvén waves and drift-acoustic waves.

In uniform plasmas, ion acoustic waves and shear Alfvén waves (SAW) represent distinct branches of the low-frequency spectrum with electrostatic and transverse electromagnetic polarization, respectively. In inhomogeneous plasmas, wave properties can be modified quantitatively and qualitatively, (i) ion acoustic waves, modified by diamagnetic drift frequencies, becomes drift-acoustic waves [1], while maintaining dominantly electrostatic perturbations. (ii) When a wave experiences a periodic index of refraction, distinct weakly damped eigenmodes can emerge in spectral gaps, such as Alfvén eigenmodes (AE) associated with toroidicity (TAE), reversed-shear (RSAE), or beta (BAE), assumed to possess SAW polarization. [2–10]. (iii) Importantly, theory predicts SAW and drift-acoustic wave branches can also couple, known as drift-Alfvén waves, exhibiting a mixture of electrostatic and electromagnetic perturbations [11–13]. The electrostatic-electromagnetic mixture is the wave 'polarization'. Drift-Alfvénic waves play crucial roles in both space and fusion plasmas, influencing turbulence, heat and particle transport, magnetic reconnection, and wave-particle interaction. They directly impact the safety of spacecraft and the performance of fusion devices [14,15].

Despite their significance, drift-Alfvén waves have never been unambiguously identified in fusion experiments, due to the inability to measure the polarization. In this Letter, a novel method is developed from gyrokinetic theory [16] to estimate drift-Alfvén wave polarization from fluctuations of electron temperature δT_e and density δn_e, quantities that are readily measured. For the first time, drift-Alfvén waves are clearly identified among various instabilities that are observed in the DIII-D tokamak.

Gyrokinetic theory.—In the small gyroradius (drift-kinetic) limit, the perturbed electron distribution δF_e is given by [16]

$$\delta F_e = \frac{e}{T_e} F_{0e} \delta\phi_\parallel + \frac{e}{m_e} \frac{\hat{\omega}_*}{\omega} F_{0e} \delta\psi + \delta K_e, \qquad (1)$$

where the unperturbed distribution F_{0e} is taken to be a Maxwellian, $\delta\phi_\parallel = \delta\phi - \delta\psi$ is the effective parallel electric potential, $\delta\phi$ is the scalar potential, $\delta\psi = \omega\delta A_\parallel/ck_\parallel$, with $\delta A_\parallel$ and $k_\parallel$ being, respectively, the parallel components of the vector potential $\delta\mathbf{A}$ and wave vector $\mathbf{k}$, and $\hat{\omega}_* F_{0e} = (\mathbf{k} \times \hat{b}/\Omega) \cdot \nabla F_{0e}$. (Here, ω is the wave frequency, Ω is the electron cyclotron frequency, and $\hat{b}$ is the magnetic field unit vector.) Note that, since $|\omega/kv_A|^2 \ll 1$ with v_A being the Alfvén speed and $\beta \ll 1$, the perturbed magnetic compression $\delta B_\parallel$ is assumed negligible, i.e., $\delta A \approx \delta A_\parallel$. Here, β is the ratio between thermal plasma pressure and magnetic field pressure.

Meanwhile, in Eq. (1), δK_e depends on whether electrons are circulating or magnetically trapped. For circulating electrons with thermal speed v_{te} in a low-frequency

wave, $\delta K_{e,c} \sim O(|\omega/k_\parallel v_{te}|) \ll 1$ and is negligible. For trapped electrons, however, we have, in the $\omega/\omega_{be} \ll 1$ limit,

$$\delta K_{e,t} = -\frac{e}{T_e}\frac{(\omega - v_{te}^2\hat{\omega}_*)F_{0e}}{\omega - \bar{\omega}_{de}}\left(\overline{\delta\phi_\parallel} + \frac{\overline{\omega_d\delta\psi}}{\omega}\right), \quad (2)$$

where ω_{be} is the electron magnetic bounce frequency, $\omega_{de} = \mathbf{k}_\perp \cdot \mathbf{v}_d$, with $\mathbf{v}_d = \hat{b} \times (v_\perp^2/2 + v_\parallel^2)\vec{\kappa}/\Omega$ ($\vec{\kappa} = \hat{b} \cdot \nabla\hat{b}$ is the curvature), and $\bar{A}$ denotes bounce averaging of A. From Eqs. (1) and (2), we can then express $\delta n_e = \int d^3v \delta F_e \equiv \langle \delta F_e \rangle_v$, $\delta P_e = m_e\langle (v^2/2)\delta F_e \rangle_v$ and $\delta T_e = (\delta P_e - T_e\delta n_e)/n_e$ in terms of $\delta\phi_\parallel$ and $\delta\psi$ in order to derive the potentials, $\delta\phi_\parallel$ and $\delta\psi$, in terms of $\delta n_e/n_e$ and $\delta T_e/T_e$. The resultant expressions, however, can be simplified by noting that AEs typically have $|\omega| \gtrsim |v_{te}^2\hat{\omega}_*| > |\omega_{de}|$ and $|k_\parallel qR| < 1$, with qR being the connection length. Thus $\overline{\delta\phi} \approx \delta\phi$ and, in the lowest order, $\delta K_{e,t}$ can be approximated as

$$\delta K_{e,t} \approx -\frac{e}{T_e}\left(1 - \frac{v_{te}^2\hat{\omega}_*}{\omega}\right)F_{0e}\delta\phi_\parallel. \quad (3)$$

From Eqs. (1)–(3), one finds that

$$\frac{\delta n_e}{n_e} = \frac{e}{T_e}\left[\left(1 - f_T + f_T\frac{\omega_{*e}}{\omega}\right)\delta\phi_\parallel + \frac{\omega_{*e}}{\omega}\delta\psi\right], \quad (4)$$

where f_T is the trapped-electrons fraction, with $f_T \simeq \sqrt{2\varepsilon}$ in the circular cross-section approximation. Here $\omega_{*e} = (k_\theta cT_e/eB)(\nabla\ln n_e)$ is the electron diamagnetic drift frequency. Note that the trapped-electron contributions are to be evaluated at the low field side of the midplane, where f_{tr} peaks. Meanwhile, $\delta T_e/T_e$ can be shown to be

$$\frac{\delta T_e}{T_e} = \left(\eta_e\frac{\omega_{*e}}{\omega}\right)(f_T\delta\phi_\parallel + \delta\psi)\frac{e}{T_e}. \quad (5)$$

Here, $\eta_e = \nabla\ln T_e/\nabla\ln n_e$. Equations (4) and (5) yield

$$\frac{e\delta\phi_\parallel}{T_e} = \frac{1}{1 - f_T}\left(\frac{\delta n_e}{n_e} - \frac{\delta T_e}{\eta_e T_e}\right), \quad (6)$$

$$\frac{\delta\phi_\parallel}{\delta\psi} = \frac{(\omega_{*e}/\omega)(\delta n_e/n_e - \delta T_e/\eta_e T_e)}{(1 - f_T)(\delta T_e/\eta_e T_e) + f_T(\omega_{*e}/\omega)(\delta T_e/\eta_e T_e - \delta n_e/n_e)}. \quad (7)$$

Recalling that $\delta\phi_\parallel$ and $\delta\psi$ correspond to perturbations in the parallel electric field and in the perpendicular magnetic field, Eq. (7) represents the ratio between drift-acoustic and shear-Alfvénic fluctuations. Note that this method is quite general and applicable to all waves with frequencies smaller than the ion cyclotron frequency, the frequencies of compressional Alfvén waves, and $k_\parallel v_{te}$. However, it is
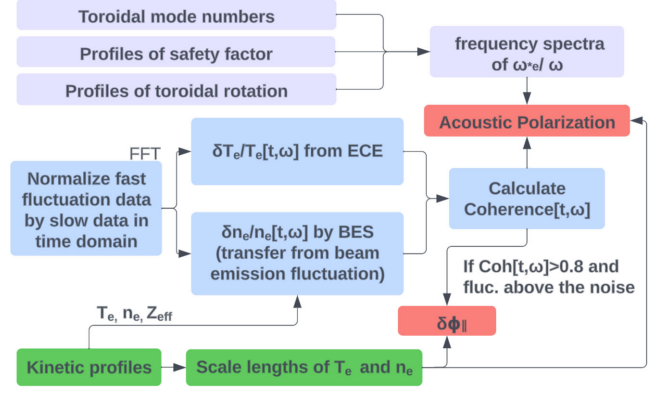

FIG. 1. Flow chart for the calculation of $\delta\phi_\parallel$ and polarization.

not suitable for application to zonal modes with poloidal and toroidal mode numbers $m = n = 0$, such as geodesic acoustic modes (GAM).

It is also instructive to analyze the polarization using the electron fluid description. Here, we assume that trapped electron effects are negligible and consider only circulating electrons. From the continuity equation, we have $\delta n_e + \xi_{e,r}\nabla n_e + n_e\nabla \cdot \vec{\xi}_e = 0$, where $\vec{\xi}_e$ is the displacement of the electron fluid by the wave. Meanwhile, with $\omega/k_\parallel v_{te} \ll 1$, circulating electrons are isothermal, so $\delta T_e + \xi_{e,r}\nabla T_e = 0$. Now thermal electrons follow the field lines so $\hat{b} \cdot \nabla\xi_{e,r} = \delta B_r/B$ or $\xi_{e,r} = -k_\theta\delta A_\parallel/k_\parallel B = -(ck_\theta/\omega B)\delta\psi$. Hence,

$$-\nabla \cdot \vec{\xi}_e = \frac{\delta n_e}{n_e} - \frac{\delta T_e}{\eta_e T_e}, \quad (8)$$

$$\frac{\delta T_e}{T_e} = \eta_e\frac{\omega_{*e}}{\omega}\frac{e\delta\psi}{T_e}. \quad (9)$$

In the limit of $f_T \to 0^+$, Eq. (5) reduces to Eq. (9). Equations (6) and (8) imply that the electron density compression is $-\nabla \cdot \vec{\xi}_e = e\delta\phi_\parallel/T_e$, as expected for ion-acoustic fluctuations. In this Letter, polarization is defined as $\delta\phi_\parallel/(\delta\phi_\parallel + \delta\psi)$, quantified from Eqs. (6) and (7) using experimental data.

Measurements of drift-Alfvén wave polarization.—The $\delta\phi_\parallel$ and polarization of TAE, RSAE, low-frequency mode (LFM) [17–28] and fishbones [29] in reversed-shear, L-mode, DIII-D plasmas is assessed. The gradient scale length parameter η_e at the mode location is measured by Thomson scattering [30], $\delta T_e/T_e$ is measured by electron cyclotron emission (ECE) [31], and $\delta n_e/n_e$ is measured by beam emission spectroscopy (BES) [32] and, in the case of weak density fluctuations, is estimated from line-averaged density measurements by the more sensitive radial inter-ferometer-polarimeter (RIP) system [33]. The calculation of $\delta\phi_\parallel$ is summarized in Fig. 1.

According to Eq. (6), for electromagnetic polarization with $\delta\phi_\parallel = 0$, the ratio of $\delta T_e/T_e$ to $\delta n_e/n_e$ should equal η_e. In this case, δT_e and δn_e are caused by radial displacement of field lines, so δT_e and δn_e are determined by $\xi_{e,r}$ and radial gradients of T_e and n_e. In contrast, a drift-acoustic wave does not perturb magnetic field lines, but has finite parallel electric field due to $\delta\phi_\parallel$, thus leading to finite plasma compression along B. Thus, a direct comparison of $(\delta T_e/T_e)/(\delta n_e/n_e)$ with η_e reveals whether the polarization is Alfvénic or not.

In experiment, it is found that the relation of $(\delta n_e/n_e)/(\delta T_e/T_e)$ to $1/\eta_e$ strongly varies, depending on the waves studied. As one typical example, Fig. 2 shows that the $\delta n_e/n_e$ induced by RSAEs is $\sim 7 \times 10^{-4}$, while $\delta T_e/T_e$ is $\sim 2.5 \times 10^{-3}$ when RSAE frequency sweeping begins; so $\delta T_e/T_e$ is ~ 3–4 times larger than $\delta n_e/n_e$, which are the same order of magnitude documented in [34]. This is close to the η_e value of ~ 3.3, implying that these RSAEs have dominant electromagnetic polarization. Analysis of 485 RSAE cases show that this is a typical result [Fig. 2(e)].

Notice in Fig. 2(b) that $\delta T_e/T_e$ steadily decreases but $\delta n_e/n_e$ is nearly constant as the RSAE frequency sweeps up from the GAM frequency towards the TAE. As a result, $(\delta T_e/T_e)/(\delta n_e/n_e)$ increases towards η_e, as the frequency increases, exhibiting more electromagnetic polarization and less electrostatic polarization. This is consistent with the NOVA-K [35] prediction that, as the frequency sweeps up and the minimum safety factor $q_{\min}$ decreases, the RSAE decouples from the GAM, but starts to couple to TAE [36]. Note that the reduced $\delta T_e/T_e$ is not caused by changes in plasma profiles, since the timescale of RSAE frequency sweeping is only ~ 10 ms, much shorter than the confinement time.

For the LFM with the "Christmas light" pattern [25] in Fig. 2(d), $\delta T_e/T_e$ is as large as $\sim 1\%$, ~ 4 times stronger than for RSAEs, even though η_e is similar in value to the RSAE cases [Fig. 2(e)]. However, $\delta n_e/n_e$, induced by LFM, is even below the noise level of the BES system of $\sim 3 \times 10^{-4}$ at the frequency range of interest in this shot. The line-averaged fluctuation $\delta\bar{n}_e/\bar{n}_e$ observed by the sensitive RIP diagnostic is only $\sim 3\%$ of the measured $\delta T_e/T_e$ [Fig. 2(c)], a striking difference from the RSAE case. In contrast, for BAEs, $\delta n_e/n_e$ is comparable to LFM levels, but $\delta T_e/T_e$ is much smaller [Figs. 2(c),2(d)]. This observation strongly suggests that LFMs have a much larger $\delta\phi_\parallel$ than RSAEs or BAEs.

The $\delta\phi_\parallel$ is quantified, when the coherence of $\delta T_e/T_e$ and $\delta n_e/n_e$ are above 0.8 and when both amplitudes are well above the diagnostic noise floor (Fig. 1). Figures 3(a) and 3(c) show the coherence spectra of $\delta T_e/T_e$ and $\delta n_e/n_e$ for RSAE and LFM, respectively. It should be noted that, for BES, the mode amplitudes of LFM are near noise levels and barely detectable. Therefore a lower bound of $\delta\phi_\parallel$ is estimated from the BES data.
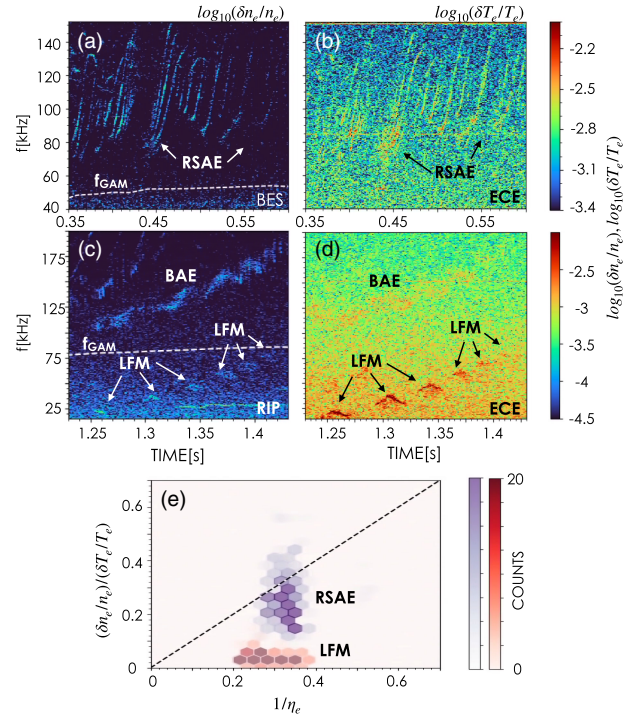

FIG. 2. Frequency spectra of (a) $\delta n_e/n_e$ measured by BES channel 46 at $R = 1.978$ m and (b) $\delta T_e/T_e$ measured by ECE channel 15 at $R = 1.97$ m in shot 178 631; (c) $\delta n_e/\bar{n}_e$ measured by RIP, and (d) $\delta T_e/T_e$ measured by ECE in shot 178633. The upper color bar is for (a) and (b); the lower color bar is for (c) and (d). GAM frequencies are shown as dashed lines in (a) and (c). (e) 2D histogram depicting the ratio of $\delta n_e/n_e$ and $\delta T_e/T_e$ to $1/\eta_e$ for 485 RSAEs (purple) and 339 LFMs (red), binned into 25×25 grids ranging from 0 to 1. Standard deviation of $1/\eta_e$ is 0.032 for RSAE and 0.044 for LFM. Standard deviation of $(\delta n_e/n_e)/(\delta T_e/T_e)$ is 0.08 for RSAE and 0.022 for LFM.

Owing to the balance between $(\delta T_e/T_e)/(\delta n_e/n_e)$ and η_e, $\delta\phi_\parallel$ of RSAEs is generally small [Fig. 3(b)] although, as discussed above, $\delta\phi_\parallel$ is noticeably larger at the start of the frequency sweep when $f \simeq 70$ kHz. This can be further seen from the dashed line in Fig. 3(e), which is a fitted line to the averaged value of $\delta\phi_\parallel$ over every ~ 10 kHz in the frequency spectra of Fig. 3(b). In this case, $\delta\phi_\parallel$ of RSAE decreases from 1.14 V at 75 kHz to 0.3 V at 143 kHz, with a sharp drop by 0.35 V at 95 kHz.

In contrast, $\delta\phi_\parallel$ of LFM is significantly larger than that of RSAE [Fig. 3(d)]. The averaged value of $\delta\phi_\parallel$ at the lower-bound of the measurement is 5.5 V at 56 kHz and 3.5 V at 104 kHz, which is roughly 1 order of magnitude larger than $\delta\phi_\parallel$ of RSAEs [Fig. 3(e)]. In addition, the $\delta\phi_\parallel$ of LFM below 70 kHz is estimated, using the line-averaged $\delta\bar{n}_e/\bar{n}_e$ measured by the RIP system. The results suggest a $\delta\phi_\parallel$ of ~ 10 V in the low-frequency range [Fig. 3(e)]. The $\delta\phi_\parallel$ of TAE at the plasma edge is also included in Fig. 3(e), using the local $\delta n_e/n_e$ measured by BES. The $\delta\phi_\parallel$ of TAE is comparable to RSAE values.
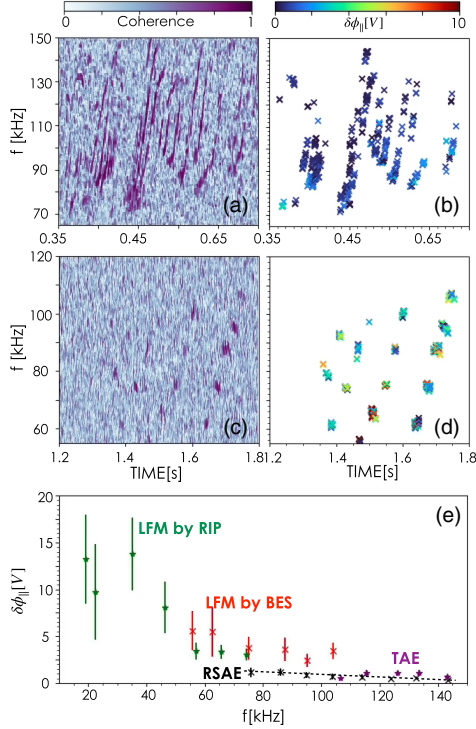
FIG. 3. Coherence of spectra between ECE δT_e and BES δn_e for (a) RSAE from shot 178 631 and (c) LFM from shot 132 710. The calculated $\delta\phi_\parallel$ from Eq. (6) in the time-frequency domain for (b) RSAE and (d) LFM. (e) $\delta\phi_\parallel$ averaged over every 10 kHz for LFM using δn_e measured by RIP (green), and by BES for LFM (red), RSAE (black), and TAE (purple).

To quantify the polarization from Eqs. (7), knowledge of k_θ and ω is required for ω_{*e}/ω. The analysis proceeds as in Fig. 1, with the following subtleties. (i) The implied mode frequency ω is in the plasma frame, i.e., $\omega = \omega_{\text{lab}} - n\omega_{\text{rot}}$, as a function of toroidal mode number n. Here, ω_{rot} is the angular frequency of toroidal rotation of carbon, measured by charge exchange recombination spectroscopy [37]. (ii) For RSAE, n is derived from the phase variation over an array of toroidal magnetic loops that are located on the outer midplane of the torus. The poloidal mode number m is estimated by nq, where q is the safety factor. The time evolution of q profiles is obtained by EFIT equilibrium reconstruction, utilizing external magnetic fields at the first wall and internal magnetic fields, measured using the motional Stark effect [38]. For LFM, magnetic perturbations have never been detected by magnetic loops on the wall across the DIII-D database and the internal magnetic perturbation, measured by RIP, is not observed or, in other words, significantly smaller than that induced by BAE. Nevertheless, the Christmas light pattern determines a unique set of (m, n) assignments from the time evolution of q_{min} (minimum of the safety factor), based on the assumption that the modes occur at rational values of q_{min} [25]. The assigned mode numbers are labeled in Fig. 4(b). With the knowledge of m, k_θ is estimated from
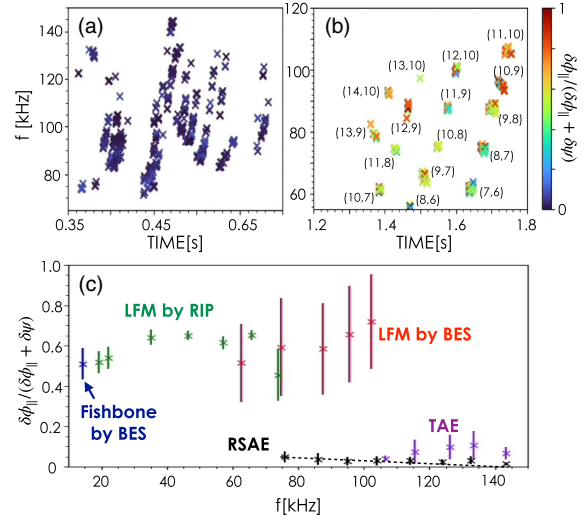

FIG. 4. Frequency dependence of polarization of (a) RSAE in shot 178 631 and (b) LFM in shot 132 710. The poloidal m and toroidal n numbers are labeled in (m, n) format in (b). (c) Polarization, which is averaged over every 10 kHz for LFM using δn_e measured by RIP (green) and by BES for LFM (red), RSAE (black), TAE (purple), and fishbone (blue).

gm/r, where $g = 0.75$ is a geometrical correction factor that takes into account the difference between real geometry coordinates and flux coordinates [25].

The time evolution of polarization of RSAE and LFM as a function of frequency appears in Figs. 4(a) and 4(b), respectively. The polarization of RSAE is, in general, negligibly small, consistent with SAW polarization [Fig. 4(a)]. The averaged value over every 10 kHz shows polarization gradually decreases from ~0.1 to ~0, as the frequency sweeps up [dashed line in Fig. 4(c)]. This is consistent with a small gradual decrease of $\delta\phi_\parallel$, as discussed previously.

On the other hand, LFM exhibits a significantly larger electrostatic polarization at all frequencies. Moreover, the measured polarization exhibits rapid changes throughout its short lifetime, as seen from the overplotted crosses in Fig. 4(b) for each set of mode numbers. This is considered to be related to the spatial resolutions of diagnostic systems, discussed in detail later. The polarization of LFM, which uses $\delta n_e/n_e$ measured by BES and RIP, is about 0.6. Both cases exhibit larger or comparable electrostatic components, compared to electromagnetic components. The electrostatic polarization of TAE and fishbone is also estimated and the averaged value is overlaid for comparison in Fig. 4(c).

Discussion.—It is noteworthy that the standard deviation of LFM polarization measured by BES [see the error bars of Fig. 4(c)] is notably larger than those of RSAE, TAE, fishbone, and LFM measured by RIP. A detailed examination of the raw data reveals that this is primarily attributed to the rapid temporal evolution of fluctuations.
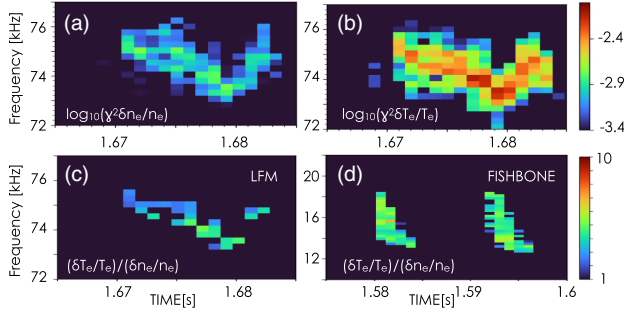
FIG. 5. LFM of $m = 8/n = 7$ from Fig. 4(b) is investigated in detail. Time evolution of $\gamma^2 \delta n_e/n_e$ (a) and $\gamma^2 \delta T_e/T_e$ (b) of the LFM. γ is the coherence between δT_e and δn_e. Fluctuation ratio of (c) LFM in shot 132 710 and (d) fishbone in shot 178 631.

For instance, $\delta T_e/T_e$ increases rapidly, while the $\delta n_e/n_e$ remains nearly constant [Figs. 5(a) and 5(b)]. This corresponds to a rapid change of fluctuation ratio [Fig. 5(c)], leading to a decrease in the calculated polarization from ~ 0.9 at 1.672 s to ~ 0.4 at 1.68 s within ~ 8 ms. In contrast, the fluctuation ratio of fishbone remains nearly constant throughout the burst [Fig. 5(d)], even though the amplitudes increase as the frequencies chirp down.

This observation carries significant implications that are consistent with the expected characteristics of drift-Alfén waves: (i) Theory [21,27,28] predicts negligible electrostatic polarization for the primary Alfvén wave at rational surface $q = m/n$, but electrostatic sidebands at $q = (m \pm 1)/n$. (2) δn_e measured by BES [32] and δT_e measured by ECE [31] have finite radial spatial resolutions of ~ 3.9 and 1.9 cm in shot 132 710, respectively, measuring near the peak positions of the modes. The resolutions do not vary across the frequency domain. The radial differences of δn_e and δT_e is less than 1 cm, much smaller than the ~ 10 cm radial extension of the mode structures. The measurements span multiple rational surfaces and likely average over both sidebands and the primary rational surface. (iii) As q decreases over time, BES and ECE weight the primary Alfvén waves and acoustic sidebands differently, resulting in a prompt change in the measured mode polarization; in contrast, RIP, which measures line-integrated perturbations that always include the sidebands [33], finds small variations in polarization. (iv) With increasing mode number, the LFM polarization increases [Figs. 4(b) and 4(c)] but the LFM amplitude decreases [Fig. 7(a) of [25] and Fig. 5(a) of [18]]. It is speculated to be due to increased ion Landau damping associated with stronger electrostatic drift-acoustic fluctuations. These measurements will be compared to various numerical codes for data interpretation and model validation, through synthetic diagnostics with analogous radial averaging in future studies.

In summary, we present the first experimental identification of drift-Alfvén waves through the measurement of a mixture of electrostatic and electromagnetic perturbations, referred to as "polarization." The breakthrough is enabled by a novel methodology developed from gyrokinetic theory, using routinely measured quantities such as δT_e and δn_e. In the future, the measurement will be expanded to the high-field side and other plasma regions with improved diagnostic spatial resolution. More importantly, this innovative method will be applied to investigate various high-n turbulence and wide variety of low-frequency modes in magnetic confinement experiments, shedding light on the nature of their perturbations.

[*]Corresponding author: duxiaodi@fusion.gat.com

[1] N. A. Krall and A. W. Trivelpiece, *Principles of Plasma Physics* (McGraw-Hill, New York, 1973), Eq. (4.14.14).

[2] W. W. Heidbrink and G. J. Sadler, Nucl. Fusion **34**, 535 (1994).

[3] A. Fasoli, C. Goremnzano, H. L. Berk *et al.*, Nucl. Fusion **47**, S264 (2007).

[4] W. W. Heidbrink, Phys. Plasmas **15**, 055501 (2008).

[5] B. N. Breizman and S. E. Sharapov, Plasma Phys. Controlled Fusion **53**, 054001 (2011).

[6] K. Toi, K. Ogawa, M. Isobe, M. Osakabe, D. A. Spong, and Y. Todo, Plasma Phys. Controlled Fusion **53**, 024008 (2011).

[7] N. N. Gorelenkov, S. D. Pinches, and K. Toi, Nucl. Fusion **54**, 125001 (2014).

[8] L. Chen and F. Zonca, Rev. Mod. Phys. **88**, 015008 (2016).

[9] K. Mcclements and E. D. Fredrickson, Plasma Phys. Controlled Fusion **59**, 053001 (2017).

[10] Y. Todo, Rev. Mod. Plasma Phys. **3** (2019).

[11] J. T. Tang and N. C. Luhmann, Jr., Phys. Fluids **19**, 1935 (1976).

[12] L. Chen, J. Y. Hsu, P. K. Kaw, and P. H. Rutherford, Nucl. Fusion **18**, 1371 (1978).

[13] F. Zonca and L. Chen, Phys. Plasmas **21**, 072120 (2014).

[14] W. Horton, Phys. Rep. **192**, 1 (1990).

[15] W. Horton, Rev. Mod. Phys. **71**, 735 (1999).

[16] L. Chen and A. Hasegawa, J. Geophys. Res. **96**, 1503 (1991).

[17] N. Gorelenkov, H. Berk, E. Fredrickson, and S. Sharapov (JET EFDA Contributors), Phys. Lett. A **370**, 70 (2007).

[18] N. N. Gorelenkov, M. A. V. Zeeland, H. L. Berk, N. A. Crocker, D. Darrow, E. Fredrickson, G. Y. Fu, W. W. Heidbrink, J. Menard, and R. Nazikian, Phys. Plasmas **16**, 056107 (2009).

[19] I. Chavdarovski and F. Zonca *et al.*, Phys. Plasmas **21,** 052506 (2014).

[20] H. S. Zhang, Y. Q. Liu, Z. Lin, and W. L. Zhang, Phys. Plasmas **23,** 042510 (2016).

[21] Y. Liu, Z. Lin, H. Zhang, and W. Zhang, Nucl. Fusion **57,** 114001 (2017).

[22] L. Chen and F. Zonca, Phys. Plasmas **24,** 072511 (2017).

[23] C. Z. Cheng, G. J. Kramer, M. Podesta, and R. Nazikian, Phys. Plasmas **26,** 082508 (2019).

[24] G. J. Kramer, C. Z. Cheng, M. Podestà, and R. Nazikian, Plasma Phys. Controlled Fusion **62,** 075012 (2020).

[25] W. W. Heidbrink, M. A. Van Zeeland, M. E. Austin, A. Bierwage, L. Chen, G. J. Choi, P. Lauber, Z. Lin, G. R. McKee, and D. A. Spong, Nucl. Fusion **61,** 016029 (2021).

[26] G. J. Choi *et al.*, Nucl. Fusion **61,** 066007 (2021).

[27] R. R. Ma, L. Chen, F. Zonca, Y. Li, and Z. Qiu, Plasma Phys. Controlled Fusion **64,** 035019 (2022).

[28] R. R. Ma, W. W. Heidbrink, L. Chen, F. Zonca, and Z. Qiu, Phys. Plasmas **30,** 042105 (2023).

[29] Liu Chen, R. B. White, and M. N. Rosenbluth, Phys. Rev. Lett. **52,** 1122 (1984).

[30] T. N. Carlstrom *et al.*, Rev. Sci. Instrum. **63,** 4901 (1992).

[31] M. E. Austin and J. Lohr, Rev. Sci. Instrum. **74,** 1457 (2003).

[32] G. Mckee, R. Ashley, R. Durst, R. Fonck, M. Jakubowski, K. Tritz, K. Burrell, C. Greenfield, and J. Robinson, Rev. Sci. Instrum. **70,** 913 (1999).

[33] J. Chen, W. X. Ding, D. L. Brower, D. Finkenthal, C. Muscatello, D. Taussig, and R. Boivin, Rev. Sci. Instrum. **87,** 11E108 (2016).

[34] M. A. Van Zeeland, G. J. Kramer, M. E. Austin, R. L. Boivin, W. W. Heidbrink, M. A. Makowski, G. R. McKee, R. Nazikian, W. M. Solomon, and G. Wang, Phys. Rev. Lett. **97,** 135001 (2006).

[35] C. Z. Cheng, Phys. Rep. **211,** 1 (1992).

[36] M. A. Van Zeeland, M. E. Austin, N. N. Gorelenkov, W. W. Heidbrink, G. J. Kramer, M. A. Makowski, G. R. McKee, R. Nazikian, E. Ruskov, and A. D. Turnbull, Phys. Plasmas **14,** 056102 (2007).

[37] C. Chrystal, K. H. Burrell, B. A. Grierson, S. R. Haskey, R. J. Groebner, D. H. Kaplan, and A. Briesemeister, Rev. Sci. Instrum. **87,** 11E512 (2016).

[38] F. M. Levinton, R. J. Fonck, G. M. Gammel, R. Kaita, H. W. Kugel, E. T. Powell, and D. W. Roberts, Phys. Rev. Lett. **63,** 2060 (1989).